ACS Sustainable Chemistry & Engineering

Research Article

Cite This: ACS Sustainable Chem. Eng. 2019, 7, 14765−14774

pubs.acs.org/journal/ascecg

Strong Silk Fibers Containing Cellulose Nanofibers Generated by a Bioinspired Microfluidic Chip

Li Lu,[†] Suna Fan,[†] Qianqian Niu,[†] Qingfa Peng,[†,∥] Lihong Geng,[‡] Gesheng Yang,[†] Huili Shao,[†] Benjamin S. Hsiao,*[,§] and Yaopeng Zhang*[,†]

[†]State Key Laboratory for Modification of Chemical Fibers and Polymer Materials, Shanghai Belt and Road Joint Laboratory of Advanced Fiber and Low-Dimension Materials, College of Materials Science and Engineering, Donghua University, 2999 North Renmin Road, Songjiang, Shanghai 201620, P. R. China

[‡]Key Laboratory of Polymer Materials and Products of Universities in Fujian, Fujian University of Technology, 33 Xuefu South Road, New University District, Fujian 350118, P. R. China

[§]Department of Chemistry, Stony Brook University, Stony Brook, New York 11794, United States

Supporting Information

ABSTRACT: As spider silks have extraordinary mechanical properties, the design of high-performance artificial silk fibers has been one of the focuses in the field of biomimetic fibers. Cellulose nanofibers (CNFs) have considerable potential being an effective reinforcing agent in biocompatible composites because of their high aspect ratio, good stiffness of the crystalline regions, and biocompatibility. In this study, regenerated silk fibroin (RSF)/CNF hybrid fibers were dry-spun through a microfluidic chip, which mimicked the shape of spider's major ampullate gland. The results showed that the presence of CNF can substantially enhance the mechanical properties of RSF. In specific, the breaking strength of the RSF/CNF fibers with 0.1 wt % CNF was increased to 486 ± 106 MPa with a maximum value of 686 MPa, significantly higher than that of silk fibers from silkworm. The enhancement could be attributed to higher orientation of crystalline and mesophase contents, higher crystallinity, and hydrogen bonds linked between RSF and CNF. This study outlined a simple and environmentally friendly pathway to generate artificial silks with high-performance properties.

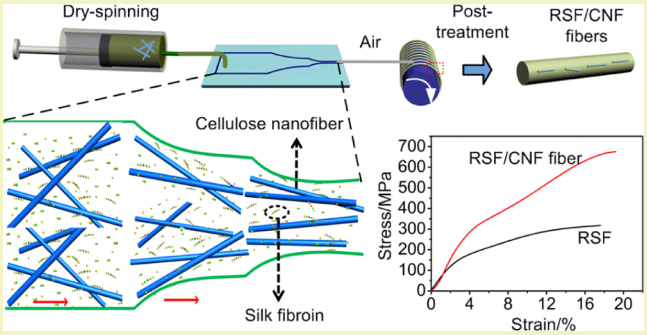

KEYWORDS: *regenerated silk fibroin, cellulose nanofibers, dry-spinning, microfluidic chip, mechanical properties*

INTRODUCTION

Spider silks have attracted a great deal of attention because of their extraordinary mechanical properties. As a result, these materials have shown great potential in various biomedical and industrial applications.[1,2] Spiders employed with different combinations of silk proteins can produce different types (up to seven) of silk. However, such production cannot be easily scaled up because of the highly cannibalistic and territorial behavior of spiders.[2,3] Silkworm silk is considerably weaker than spider's dragline silk. However, fibers obtained by force-reeling directly from silkworms can possess good mechanical properties approaching that of spider silks.[4,5] The silk fibers from silkworm, often considered as the "queen of textiles", are plentiful in supply and can be produced on a commercial scale with a quantity of hundreds of thousands of tons per year; the production quantity of reelable silkworm cocoons in 2017 was 592 967 tons (China alone 398 215 tons, almost 70% of the whole quantity).[6,7] Therefore, the design and production of artificial high-performance silk through biomimetic spinning has attracted great interest from academic to industrial laboratories.[8−11]

The current spinning processes for artificial silks include wet spinning,[4,8,9] electrospinning,[12,13] and dry spinning.[11,14,15] The processes of wet spinning and electrospinning require the precipitation of a coagulant or the use of high electric field, which are very different from the natural process, where spider or silkworm silk proteins in the aqueous solution are transformed into solid and insoluble fibers in the atmospheric environment.[16] This process is similar to the dry-spinning approach, where fiber solidification occurs because of the water evaporation. During the natural process of forming silkworm silk and spider silk, the S-shaped duct in the spider with dimensions of only a few micrometers can further adjust the ionic conditions and pH level of silk proteins. Furthermore, the elongation flow through the duct at a low shear rate may be important to produce the uniaxial molecular orientation before the formation of spider threads.[16−21] However, there are significant differences between the shape of the *Nephila edulis*

Received: May 14, 2019
Revised: July 16, 2019
Published: August 2, 2019

DOI: 10.1021/acssuschemeng.9b02713
ACS Sustainable Chem. Eng. 2019, 7, 14765−14774

MA silk gland and *Bombyx mori* silk gland.[17,18] Silkworm glands exhibit a much different flow extension profile from spider glands. The shear flow effects are much greater in spider than in silkworm. In this scenario, microfluidic devices may be used to mimic the flow conditions in spider glands technically, and the irreversible aggregation of silk proteins can be controlled precisely for fiber formation in a few micrometers.[22,23] This technology has been the base for a few recent studies to mimic the spinning process of spider and silkworm, where microfluidic chips were used to concentrate, shear, and elongate the spinning dope.[24−28] The results from these studies indicated that the microfluidic chip could play an important role in biomimetic spinning.[29,30] However, the functions of spider's spinning apparatus have not been comprehensively imitated. For this purpose, we designed and fabricated a microfluidic chip by mimicking the geometry of a *N. edulis*' major ampullate gland and spinning duct in this study.

To improve the mechanical properties of artificial silks, many researchers have incorporated nanoscale reinforcement agents into the spinning dope, including titanium dioxide (TiO_2),[15] graphene oxide (GO),[14] carbon tube,[31] cellulose nanocrystals (CNCs),[32] etc. Recently, nanoscale cellulose materials have attracted a great deal of attention in the materials community because of their low-cost and high-performance nature.[33,34] For example, cellulose nanofibers (CNFs) can be extracted from trees and other plants and have been demonstrated excellent potentials as reinforcement agents in composites because of the high aspect ratio (>150) and high stiffness (~138 GPa) of the crystalline regions.[35] For example, Isogai et al.[36] showed that the tensile strength and elastic modulus of the polyvinyl alcohol film could be improved remarkably with 20% CNF addition. Håkansson et al.[37] further demonstrated that strong filaments with a strength up to 600 MPa could be generated by CNF alone (this fiber property was comparable to that of the strongest cellulose pulp fibers). Mittal et al.[35,38] recently demonstrated a high-performance CNF/Z-silk fiber system having a stiffness of 55 GPa, strength at break of 1015 MPa, and toughness of 55 MJ·m^{-3}. They also developed a pure CNF fiber system with even better performance (Young's modulus up to 86 GPa and tensile strength of 1.57 GPa), exceeding the mechanical properties of typical natural or synthetic biopolymeric fibrous materials.

Inspired by the properties and function obtained above involving CNF, a new regenerated silk fibroin (RSF)/CNF artificial silk fiber system was demonstrated in this study using the dry-spinning approach through a bioinspired microfluidic chip. The interactions between RSF molecules and CNF particles were found to be synergistic to induce high crystallinity and orientation even with a small crystallite size that resulted in high-performance artificial silk fibers. The investigation confirmed that CNF could play an important role in reinforcing the mechanical properties of artificial composite silk fibers. The resulting RSF/CNF fibers exhibited outstanding mechanical strength (the mean value: 486 MPa and the maximum value: 686 MPa), exceeding that of the typical natural silkworm *B. mori* silk (the mean value: 360 MPa).[39]

EXPERIMENTAL SECTION

Preparation of CNF Suspension. The CNF suspension was prepared according to the method described by Su et al.[40,41] Briefly, jute fibers (Redbud Textile Tech. Inc., Jiangsu, China) were first ground into small pieces with a 3−5 mm length, which were subsequently soaked in a 1 M NaOH aqueous solution for 1 day under stirring to remove most noncellulosic constituents. The treated jute fibers were washed several times and collected by vacuum filtration. Delignification was then carried out using the following procedures. The treated jute fibers were further immersed in a 1% (w/v) $NaClO_2$ buffer solution (based on acetic acid with the addition of sodium acetate aqueous solution to maintain the pH value around 5), where the suspension was heated at 70 °C for 3 h under stirring. The delignified jute fibers were washed several times and separated by vacuum filtration. This procedure was repeated 3 times, and the final samples were dried at 50 °C for 10 h.

The chosen CNF suspension was prepared as follows. Dried delignified jute fibers (1.0 g) were first suspended in water (90 mL), in which sodium bromide (0.10 g) and (2,2,6,6-tetramethylpiperidine-1-yl)oxyl (TEMPO) agent (0.02 g) were subsequently added. After that, 12 mM (per gram of cellulose) of sodium hypochlorite solution was added to initiate the oxidation process, and the reaction was stirred mechanically in a sealed bottle for 24 h. The pH value of the suspension was maintained between 10 and 10.5 during the reaction by the addition of sodium hydroxide aqueous solution (1 mol/L). The oxidized cellulose suspension was dialyzed in deionized water for 1 week. After the treatment, the suspension was further defibrillated with a homogenizer (Scientz-IID, Ningbo Scientz Biotechnology Co., Ltd., Ningbo, China) at the 50% output power (475 W) in an ice bath for 30 min. After mechanical defibrillation, the suspension was centrifuged at 4700*g* for 20 min where the supernatant was collected. With the above procedures, the final concentration of the suspension was 0.46 wt %, determined by the total organic carbon analyzer (Multi N/C3100, Analytik Jena, Germany).

Preparation of RSF Solution and RSF/CNF Suspensions. The RSF solution was prepared according to the method described in our previous work.[13] Briefly, *B. mori* cocoons (produced in Tongxiang, China) were degummed twice by immersing in 0.5 wt % aqueous Na_2CO_3 solutions at 100 °C for 30 min and subsequent washing with deionized water to remove sericin. After drying overnight, the degummed silk (De-silk) sample was dissolved in a 9.0 M LiBr aqueous solution at 40 °C for 2 h. The solution was then filtered and dialyzed using a cellulose semipermeable membrane (molecular weight cutoff 14 000 ± 2000, 44 μm in thickness, Yuanju Co. Ltd., Shanghai, China) against deionized water for 3 days.

The RSF/CNF suspensions were prepared as follows. When the RSF solution was concentrated to 20 wt % under forced airflow at 10 °C, a $CaCl_2$ aqueous solution of 3 M was added to obtain 1.0 mM/g calcium ion in the solution. At this point, the CNF suspension was carefully added into the RSF solution in which the only solvent of the RSF/CNF suspension in this work was deionized water. Then, the RSF/CNF spinning dope was concentrated to 45 wt % under forced airflow at 10 °C. The pH value of the solution was 6.3. The chosen mass ratios of the CNF/RSF suspensions were 0/1000, 0.5/1000, 1/1000, 2/1000, and 3/1000, respectively. The samples were designated as RSF/CNF-*X*. For example, RSF/CNF-1 means the mass ratio of CNF/RSF = 1/1000. The spinning dope was transferred to a syringe when the total weight concentration of RSF and CNF was about 45 wt %.

Microfluidic Dry Spinning. A dry-spinning apparatus (shown in Figure 1a) was designed and constructed with a progressively narrowing fluidic channel to mimic the shape of spider's major ampullate gland to fabricate silk fibers. Because of the high concentration of the spinning dope, the width of channel's shear segment was enlarged to 244 μm, which is 30 times wider than spider's spinning duct, and the depth of the channel was 150 μm.[17] The microfluidic channel was composed of three segments, including dope storage segment, elongation segment, and shear segment. The elongation curves were fitted using the second-order exponential decay function according to the shape of the lumen of *N. edulis*' major ampullate gland described by Knight and Vollrath.[17] Figure 1b shows the biomimetic microfluidic channel, which is defined as follows

$$y_1 = 648\, e^{(-152x)} + 137\, e^{(-18161x)} - 40 \quad (1)$$

DOI: 10.1021/acssuschemeng.9b02713
ACS Sustainable Chem. Eng. 2019, 7, 14765−14774

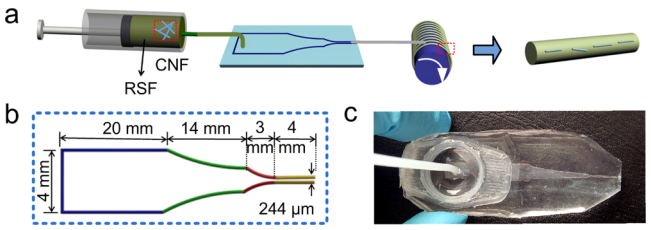

Figure 1. (a) Schematic of the dry-spinning process using a microfluidic channel; (b) dimensions of the biomimetic channel; and (c) photograph of the microfluidic chip.

$$y_2 = 12.76\, e^{(336.71x)} \quad (2)$$

where y_1 and y_2 are the half widths (μm) of the green and red channels, respectively. x is the distance (μm) from the left inlet of the channel. The photograph of the biomimetic microfluidic chip is illustrated in Figure 1c.

To generate the artificial silk fibers, the spinning dope was introduced into the microfluidic channel at a flow rate of 2 μL/min using a syringe pump (model 210P, KD Scientific Inc. USA). The distance between the spinneret and the take-up roll was 10 cm, and the spinning speed was kept at 3 cm/s. The longest continuous spinning time in our study was 33 min 12 s. The as-spun fibers with a longest length of 6 m were stored in a sealed dryer under the ambient conditions of 25 ± 2 °C and 45 ± 5% relative humidity (RH) for 48 h and then immersed in an 80 vol % ethanol aqueous solution for 3 min. Posttreatment was carried out by stretching the fiber at the draw ratios of 4 at a rate of 1 mm/s in the 80 vol % ethanol aqueous solution, and the stretched fiber was kept in the ethanol solution for 2 h at the fixed length for stabilization. The subsequent drying process was the same as the as-spun fiber to remove the residual water. De-silk fibers and post-stretched RSF fibers were also produced as two control groups.

Transmission Electron Microscopy. The morphology of CNF was characterized by JEM-2100 transmission electron microscopy (TEM). In this measurement, drops of a dilute CNF suspension (0.1 wt %) were deposited onto a glow-discharged carbon-coated copper grid. The dried specimens were then observed at 100 kV.

Atomic Force Microscopy. Atomic force microscopy (AFM) images of CNF samples were obtained using an Agilent 5500 instrument in the tapping mode at a scanning range of 1 μm and a scanning speed of 1.5 cm/s. For the AFM sample preparation, a 0.0015 wt % of CNF suspension was spin-cast onto a clean silicon wafer and dried at room temperature.

Rheological Measurement. The rheological measurements of the 45 wt % spinning dope were conducted on an RS150 rheometer (Thermo Haake, Germany) using a 20 mm parallel plate (Ti, gap 0.3 mm) at 25 °C. The viscosity was measured as a function of shear rate in the range of 0.01−100 s^{-1} (the shear time was 300 s).

Scanning Electron Microscopy. Morphology observation of the surface of the silk fibers was performed by scanning electron microscopy (SEM; Hitachi S-4800) at 10 kV. Samples were mounted onto the specimen stubs by means of a conductive double-sided adhesive tape and sputtered with gold for 50 s at low temperature.

Mechanical Properties. Instron 5565 tensile testing machine was used to measure the mechanical properties of the single fiber. In this study, post-stretched fibers were fixed in a paper frame and measured at the ambient conditions of 25 ± 2 °C and 45 ± 5% RH. The tensile experiment was carried out at an extension rate of 2 mm/min and a gauge length of 10 mm. A total of 30 single fibers for each sample were tested. The diameter (D) and birefringence of the fiber were determined by an optical microscope (BX-51, Olympus, Japan) equipped with a U-CTB Berek compensator. The diameter of each sample was obtained from more than 10 points along the fiber axis. The compensation angle (θ) of RSF/CNF fibers was measured by the U-CTB Berek compensator at room temperature. According to θ, the optical retardation coefficient (R) was obtained by checking the table of compensation angle and retardation. Then, the birefringence index (n) was calculated by $n = R/D$. At least 10 fibers were measured for each sample to obtain the average birefringence index.

Synchrotron Radiation Small-Angle X-ray Scattering. Synchrotron radiation small-angle X-ray scattering (SR-SAXS) was

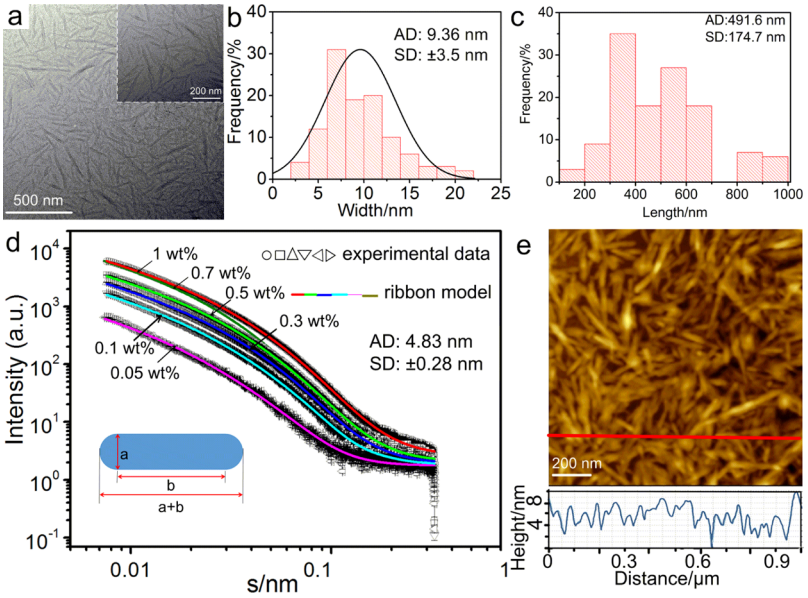

Figure 2. Morphology and size of CNF estimated by TEM, SAXS, and AFM. (a) TEM images of CNF dried from the 0.1 wt % CNF suspension at different resolutions (inset: TEM images of CNF with larger magnification). (b) Width distribution of CNF estimated from 100 different positions in (a); AD represents the average dimension and SD represents the standard deviation. (c) Length distribution of CNF estimated from 100 different positions in (a). (d) Solution SAXS profiles (intensity vs scattering vector s) and the fitting curves of CNF suspensions with concentrations of 0.05, 0.1, 0.3, 0.5, 0.7, and 1 wt %, respectively (inset: the cross-sectional shape of the ribbon model used in experimental data fitting, where AD also represents the average cross-sectional dimension and SD represents its standard deviation). (e) AFM images of CNF and the height profile along the red line in the image.

DOI: 10.1021/acssuschemeng.9b02713
ACS Sustainable Chem. Eng. 2019, 7, 14765−14774

also carried out at the BL16B1 beamline at SSRF. The chosen X-ray wavelength (λ) was 0.124 nm (energy was 10 keV). The beam spot size was 1 × 1 mm^2, and the sample-to-detector distance was 1900 mm. The exposure time for each fiber measurement was 50 s. To determine the average cross-sectional dimensions of CNF in dispersion, the exposure time of the suspension was prolonged to 300 s. Briefly, the CNF suspensions of 0.05, 0.1, 0.3, 0.5, 0.7, and 1.0 wt % were introduced into a quartz capillary and measured separately. The concentrated CNF suspension was prepared by water evaporation under forced airflow at 10 °C. A ribbon model was used to fit all scattering curves of the suspensions at different concentrations to extract the cross-sectional dimensions.[41] In site SR-SAXS was also carried out at the BL16B1 beamline at SSRF to test the shear elongation effect of the microfluidic chip. The beam spot size was 400 × 500 μm^2 and the chosen λ was 0.124 nm (energy was 10 keV), while the sample-to-detector distance was 5095 mm with an exposure time of 300 s. As polydimethylsiloxane chip has obvious X-ray absorption, we prepared a microfluidic chip sealed with bottom and upper Kapton covers as the X-ray window. A hollow microfluidic device with a channel, as shown in Figure 1, was printed by using a light-curing 3D printer (Form 2, Formlabs, USA). Then, a Kapton film was wrapped around the hollow device. A 30 wt % RSF solution was introduced into the sealed microfluidic channel at a flow rate of 50 μL/min using a syringe pump (model 210P, KD Scientific Inc. USA). The RSF solution was scanned for SAXS characterization along the flow direction in the microfluidic channel at a step of 1 mm.

Fourier Transform Infrared Spectroscopy. Infrared spectra of the single fibers of De-silk, post-stretched RSF fiber, and RSF/CNF fibers were recorded by transmission analysis with a micro-compression cell (Nicolet iN10 MX, Thermo Fisher, USA) using the wavenumber ranging from 600 to 4000 cm^{-1} at a resolution of 4 cm^{-1}, 64 scans for each spectrum, and at least 5 spectra for each sample.

X-ray Photoelectron Spectroscopy. Organic nonmetal elements were measured by an X-ray photoelectron spectroscope (ESCALAB 250Xi, Thermo Fisher Scientific), with the main tested elements such as carbon, oxygen, and nitrogen, with Al Kα (1486.8 eV) as the X-ray source, and samples were measured under an ultrahigh vacuum (<10^{-9} mbar). The samples were dried under vacuum at room temperature for 48 h in the presence of P_2O_5 before the measurements. To compensate for the surface charging effect, all binding energies were calibrated using the C (1s) carbon peak (284.8 eV).

Synchrotron Radiation Wide-Angle X-ray Diffraction. Synchrotron radiation wide-angle X-ray diffraction (SR-WAXD) was carried out at the BL15U1 beamline at the Shanghai Synchrotron Radiation Facility (SSRF). The chosen X-ray wavelength (λ) was 0.0775 nm (energy was 16 keV). The beam spot size was 3.0 × 2.5 μm^2, and the sample-to-detector distance was 1707.4 mm. The exposure time for each fiber measurement was 30 s.

RESULTS AND DISCUSSION

Characterization of CNF. Figure 2a shows the TEM images of CNF from the 0.01 wt % suspension at different magnifications, where the width and length distributions of CNF determined from the images are shown in Figure 2b,c. It was seen that the average width of CNF was about 10 nm and the average length was 491.6 ± 174.7 nm; thus, the aspect ratio of the chosen CNF was relatively large. We note that the TEM sample was prepared by evaporating the CNF suspension, so the CNF particles might have aggregates, leading to a larger width estimate. The CNF cross-sectional size was also determined by the solution SR-SAXS technique according to the method described by Su et al.[40] The results are illustrated in Figure 2d.

It was found that the ribbon model could fit all the SAXS experimental curves quite well, where the b value measured by SAXS was 4.41 ± 0.25 nm, and the average width (a + b) was 4.83 ± 0.28 nm (this was almost twice smaller than that from TEM: 9.36 ± 3.50 nm). We believe the SAXS estimate is close to the real cross-sectional dimension of CNF, as the particles are dispersed in the suspension but aggregated in the solid. The SAXS result was slightly consistent with the height estimate from the AFM measurement. From the AFM measurement of CNF (Figure 2e), the CNF particles exhibited an average height of 5 ± 2 nm, which was consistent with the SAXS results.

Rheological Behavior of the Spinning Dope. Figure 3 shows the rheological behavior of the RSF solution and

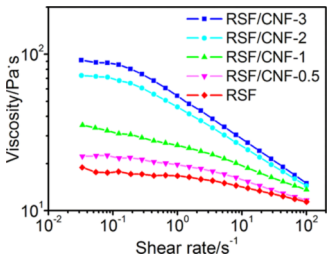

Figure 3. Rheological behavior of the RSF/CNF spinning dopes with a total weight concentration of RSF and CNF of 45 wt %.

selected RSF/CNF suspensions (the total weight concentration was kept at 45%). It was seen that the viscosity level of the RSF/CNF suspension at any given shear rate was generally higher than that of the RSF solution. This is expected as the presence of anisotropic CNF should enhance the flow resistance of the suspension mixture. It was interesting to note the zero-shear viscosity (η_0) of the mixtures increased notably with the increasing CNF content, where all RSF/CNF suspensions exhibited the shear thinning behavior. The shear thinning behavior also became more pronounced with the increase of the CNF content. This indicates that although the initial viscosity was high, it became reasonably low at high shear rate in the RSF/CNF suspension with high CNF content.

The above observation can be explained as follows. A schematic diagram illustrating the interactions between RSF and CNF is shown in Figure 4. In this diagram, the fibroin heavy chain [Protein Database (PDB) 3UA0] was chosen to represent the protein fibril model (Figure 4c) in the RSF solution. In Figure 4a, in concentrated RSF solution (45 wt %), the molecules are intertwined with each other and form an entangled network, where the entanglement points are indicated by the red dashed line circle. This solution should possess the typical viscoelastic behavior from concentrated polymer solutions. In the RSF/CNF suspension (Figure 4b), the presence of CNF with a negatively charged surface (i.e., the carboxyl groups created by the TEMPO-mediated oxidation process[36]) probably has the following roles in the hybrid RSF/CNF suspension.

First, CNF can form hydrogen bonds with RSF molecules. This interaction would stabilize the CNF dispersion in the network of RSF. Second, the presence of the sodium ions (with monovalent charge) can shield the positively charged CNF surface and cause the aggregation of CNF through hydrophobic interactions. Typically, this type of interaction would lead to weak gelation especially at higher CNF concentration. Third, the presence calcium ions (Ca^{2+} with divalent charge) in $CaCl_2$ will behave as the cross-linking agent to bind the carboxyl groups on the CNF surface and form stronger CNF

DOI: 10.1021/acssuschemeng.9b02713
ACS Sustainable Chem. Eng. 2019, 7, 14765−14774

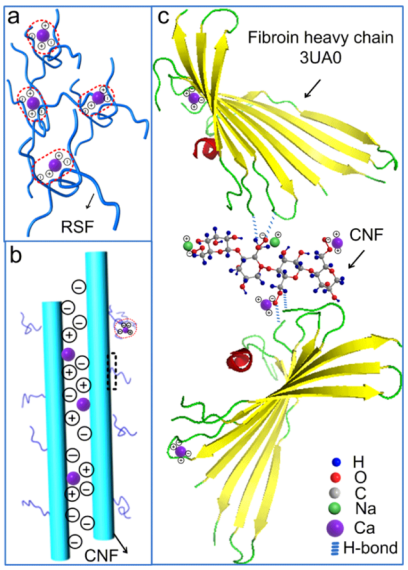

Figure 4. Schematic diagram illustrating the interactions between RSF and CNF. (a) Cross-linking points between RSF chains (in dashed red circles). (b) Interactions between RSF chains and CNFs. The blue rods represent the charged CNF containing carboxyl groups. (c) Schematic of the interfacial forces between the amino groups of RSF and carboxyl groups of CNF in the black square area in (b).

aggregation (Figure 4b,c). As the viscosity of the spinning dope increases rapidly with the CNF concentration,[42,43] we expect the last effect to be the dominant one. We note that $CaCl_2$ is a well-known weak polyelectrolyte, where Ca^{2+} can also act as a cross-linking bridge between the oxygen-containing groups on the CNF surface or RSF (Figure 4a,b).

Fiber Morphology and Mechanical Properties of Hybrid Silk Fibers. Figure 5A illustrates the typical SEM image of the RSF/CNF-1 fiber. It was found that the fiber was relatively uniform with an average diameter of about 8 μm and a smooth surface. No presence of CNF could be observed on the surface of the fiber. To determine the molecular orientation of the silk fiber, optical microscopy was also performed. Figure 5B shows the values of the birefringence index of De-silk, RSF, and RSF/CNF fibers (the detailed information can also be found in Table S1). It was seen that the values of the birefringence index of RSF/CNF fibers were all larger than that of RSF fibers (that of the RSF/CNF-1 fiber was comparable to that of De-silk). Because the birefringence index reflects the molecular orientations of both crystalline and amorphous domains, this finding indicated that the molecular orientation of the RSF/CNF fiber was higher than that of RSF fibers. The stress−strain curves of De-silk, RSF, and RSF/CNF fibers and the overview of the fiber properties are shown in Figure 5C, 5D, respectively. The detailed mechanical properties are also illustrated in Table S1. It was seen that the RSF/CNF fibers were much thinner than De-silk and RSF fibers (Table S1). The breaking stress and modulus of RSF/CNF fibers were much larger than those of De-silk and RSF fibers. This indicated that the addition of CNF notably improved the mechanical properties of regenerated silk. RSF/CNF-1 exhibited the largest average tensile strength of 487 MPa and a maximum breaking stress of 686 MPa, which was 2.5 times that of De-silk (265 MPa) and 2.2 times that of RSF fibers (307 MPa). Moreover, the breaking elongation was extended to 16%.

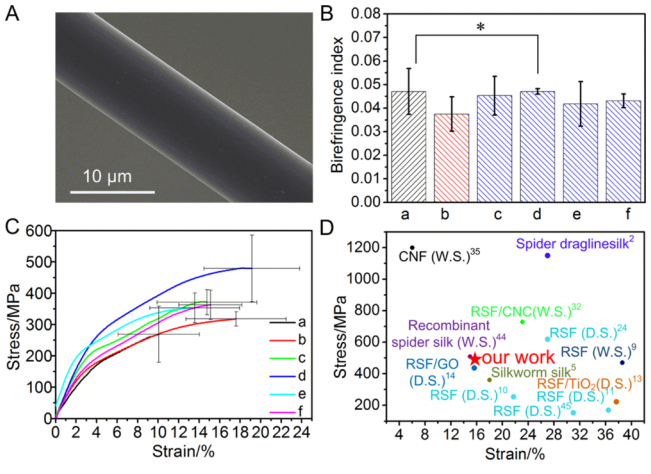

Figure 5. Morphology, structure, and properties of RSF/CNF fibers. (A) SEM image of RSF/CNF-1 fibers. (B) Birefringence index and (C) stress−strain curves of (a) De-silk, (b) RSF, (c) RSF/CNF-0.5, (d) RSF/CNF-1, (e) RSF/CNF-2, and (f) RSF/CNF-3 silk fibers (the error bars represent the standard deviations). (D) Overview of the mechanical properties of spider and RSF fibers obtained by different spinning methods[14,15,32,38,44,45] (WS: wet spinning, DS: dry spinning).

We chose the ambient conditions of 25 ± 2 °C and 45 ± 5% RH for this study because water plays a significant role in both the assembly of silk protein and formation of silk fibers. Lower humidity may facilitate the assembly of silk fibroin, more β-sheet structure, and lower degree of chain orientation and crystalline orientation and result in better mechanical properties.[10] Figure 5D further illustrates the mechanical property comparison of this work with those in the literature studies. It was found that the breaking stress of our dry-spun fibers through a microfluidic chip had already exceeded the natural cocoon silk and some hybrid dry-spun fibers, including RSF/GO fibers and RSF/TiO_2 fibers. Luo[24] prepared tough RSF silk fibers by introducing 50 wt % RSF solution into a microfluidic chip, which mimic the spinning apparatus of the silkworm. The outlet width of the microchannel was 100 μm, and the diameter of the prepared silk fibers was 2 μm. The excellent mechanical properties resulted from a bundle of fine fibers instead of an individual fiber. Compared with the wet-spinning process, the dry-spinning process does not use organic or toxic solvents and is thus environmentally friendly.

Characterization of RSF and RSF/CNF Silk Fibers. The SAXS technique was also used to characterize the structure of De-silk, RSF, and RSF/CNF-3 fibers, where the schematic representation of the SAXS setup is shown in Figure 6a and the two-dimensional (2D) SAXS patterns are shown in Figure 6b. It was seen that the De-silk possessed the least orientation, as its scattering profile was not equatorial-streak like. The one-dimensional (1D) SAXS profiles of De-silk, RSF, and RSF/CNF-3 fibers extracted along the equator are illustrated in Figure 6c, where all profiles are diffuse in nature. The interfacial property between the crystal and amorphous domains, where the scattering contrast arises, can be investigated by the Porod analysis.[46] One version of the Porod plots, $I(q)q^2-q^{-2}$, for the three fibers is illustrated in Figure 6d. In this analysis, the interface factor (σ) and the thickness of the interface zone (ΔR) can be calculated by eqs 3 and 4 from the slope (k) and intercept (b) of the $I(q)q^2-q^{-2}$ plot, which has been demonstrated in our previous work.[14]

DOI: 10.1021/acssuschemeng.9b02713
ACS Sustainable Chem. Eng. 2019, 7, 14765−14774

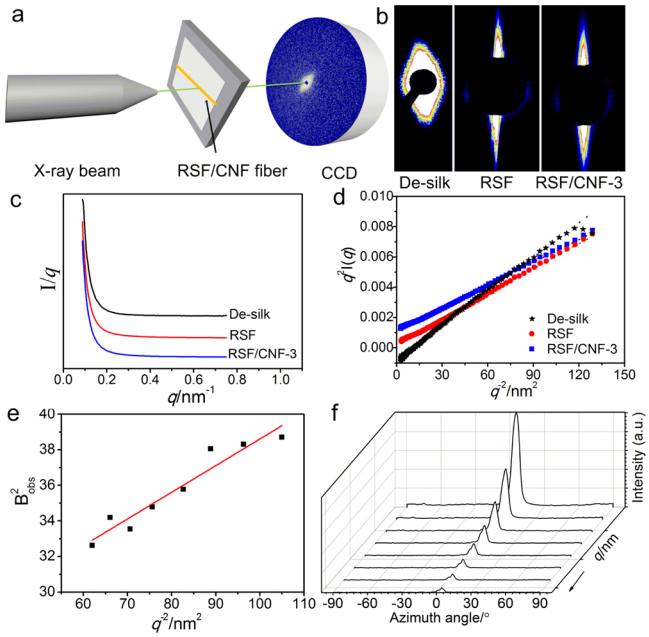

Figure 6. (a) Schematic representation of the SAXS setup, (b) 2D SAXS patterns of De-silk, RSF fibers, and RSF/CNF-3 fibers (the fiber axis is along the horizontal direction), (c) 1D equatorial scanned profiles from the 2D patterns (q is the scattering vector and $I(q)$ is the scattering intensity), (d) Porod plots of $q^2I(q)-q^{-2}$ from the profiles in (c,e) the linear fitting of the $B_{obs}{}^2-q^{-2}$ curve derived from (d), where B_{obs} is the integral breadth of the azimuthal profile, and (f) azimuthal profiles taken at different q values of the RSF/CNF fiber SAXS pattern in Figure 5b.

$$\sigma = \sqrt{b/k} \tag{3}$$

$$\Delta R = 2\sqrt{3}\sigma \tag{4}$$

On the basis of the above analysis, the σ value of the scatterer in De-silk was 1.93, and the σ values of RSF and RSF/CNF-3 fibers were 3.36 and 4.21, respectively. At the same time, the ΔR value of De-silk was 6.67 nm, and the ΔR values of RSF and RSF/CNF-3 were 11.64 and 14.58 nm, respectively. It could be concluded that the addition of CNF increased the thickness of the interface zone quite notably. Figure 6e illustrates the azimuthal profiles taken at different q value of the SAXS pattern from the RSF fiber. This breadth distribution is related to the combined effect of misorientation of the scatterer (i.e., crystalline region) and the length distribution of the anisotropic scatterer. Again, using another form of the Porod analysis,[46] the plot $B_{obs}{}^2$ versus q^{-2} can be developed and the result is shown in Figure 6f, where B_{obs} is the integral breadth of the azimuthal profile. The integral breadth of the normal of the scatterer (B_φ), which is related to the misorientation of the fibrils, and the average fibril length L can be extracted from the linear relationship of the $B_{obs}{}^2-q^{-2}$ curve, where B_φ and L could be calculated by eq 5 and (σ) using the slope (k') and intercept (b')

$$\varphi = \sqrt{b'} \tag{5}$$

$$L = 2\pi/\sqrt{k'} \tag{6}$$

The B_φ values of RSF fibers and RSF/CNF-3 fibers were found to be 10.0 and 4.9, respectively. The smaller the B_φ value, the higher the fibrillar orientation. Thus, it could be concluded that the crystal orientation of the RSF/CNF-3 fiber was larger than that of the RSF fiber. This could be attributed to the incorporation of CNF, which acted as a reinforcement additive that leads to a more orderly arrangement of the resulting silk crystalline fibrils. The L values of the RSF and RSF/CNF-3 fibers were found to be 16.2 and 11.3 nm, respectively. The small difference of the L values between the two fibers indicated that the addition of CNF had a slight effect on the formation of silk fibrils during spinning. The long rodlike CNF additive had a synergistic effect to increase the fibril orientation through shearing and elongation in the bioinspired microfluidic channel but did not affect the formation length of regenerated silk crystal fibrils.

On the basis of the above results, the following mechanism can be proposed to explain the structure formation of crystalline RSF fibrils in the suspension of RSF/CNF (the schematic diagram of the structure change in the microfluidic channel is shown in Figure 7). We believe that the initial

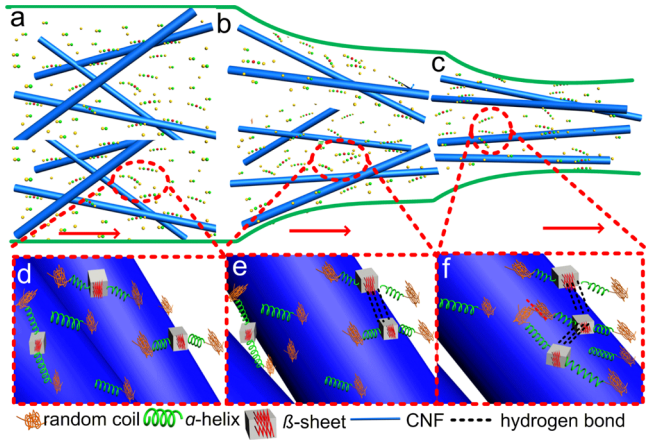

Figure 7. Illustration of the assembly process of RSF fibrils in the RSF/CNF suspension through the microfluidic channel: (a,d) RSF molecules and CNF are in the dispersion state, where most RSF molecules are in the random-coil conformation and CNFs are aggregated and only partially oriented; (b,e) CNF orientation increases and the mixture of RSF and CNF becomes relatively more homogeneous because of the shear and elongation; (c,f) both RSF molecules and CNF become highly oriented along the fiber axis, where oriented RSF fibrils are formed.

spinning dope, near the microfluidic channel entrance, contains a relatively heterogeneous structure having partially ordered CNF aggregates dispersed in a randomly oriented RSF matrix. With the gradual reduction of the channel diameter, both shear and elongation flows are imposed. The shear flow can improve the mixing process and result in a more homogeneous composite structure, where the elongation flow can increase both orientations of RSF chains and CNF aggregates. With the further reduction of the channel diameter, the increased elongation flow can greatly improve the orientation of CNF aggregates and cause the conformation changes of RSF chains because of the strong intermolecular interactions (e.g., hydrogen bonds) between RSF and CNF. The enhanced alignment of extended RSF chains would lead to the formation of RSF crystalline fibrils.

To verify the hypothesis proposed in Figure 7, the order parameter indicating the alignment and orientation of the spinning dope was characterized by SR-SAXS.[21,47] The SAXS results of the RSF solution are shown in Figure 8. The microfluidic chips have evident shear elongation effect on the

DOI: 10.1021/acssuschemeng.9b02713
ACS Sustainable Chem. Eng. 2019, 7, 14765−14774

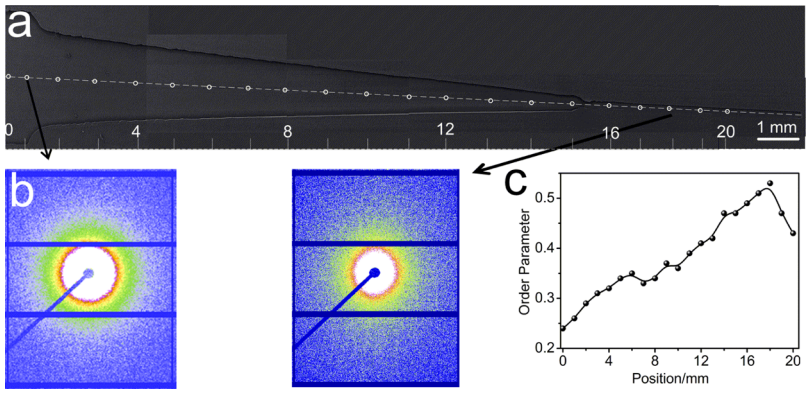

Figure 8. Alignment of RSF molecules in the microchannel. (a) Schematic of the channel geometry used for the SAXS experiments. White circles show the locations where in situ measurements were carried out. (b) μSAXS patterns at selected locations in the channel for RSF molecules. (c) Local order parameters calculated from SAXS patterns as a function of position in the channel. The locations marked with circles correspond to the data shown in (c).

solution flow through it. As the elongation curves of the microfluidic channel were fitted using the second-order exponential decay function, according to the shape of the lumen of *N. edulis*' major ampullate gland, the ordered parameters increased obviously along the gland. At the outlet, the slightly decreased order parameter indicates that the ordered molecular structure begins to decompose in a certain degree because of the straight segment.

Structural Characterization of Hybrid Silk Fibers. To further verify the hypothesis made in Figure 7, the structures of three selected fibers (De-silk, RSF, and RSF/CNF) produced from the microfluidic spinneret were characterized by Fourier transform infrared (FTIR) and WAXD measurements. The FTIR spectra and the deconvolution results of these fibers are shown in Figure 9A,B, respectively. The FTIR analysis was carried out based on Shao's assignment of the characteristic peaks for silk.[9,48−50] Briefly, for amide I, the peaks centered at 1626 and 1698 cm^{-1} can be considered as the β-sheet and β-turn structures, respectively; the broad peak between 1655 and 1660 cm^{-1} can be assigned as the random coil or the α-helical conformation or both the silk chains. For amide III, the peaks at 1233 and 1266 cm^{-1} can be assigned as the random coil/α-helix conformation and β-sheet conformation, respectively. Ling et al.[48] argued that the amide I region is not suitable for quantitative analysis because of the baseline correction problems and the atmospheric water vapor interference. However, the amide III region appears to be suitable for quantitative analysis. On the basis of this consideration, we also focused mainly on the amide III region in the study. In Figure 9A, it was found that the peak at 1233 cm^{-1} was shifted to 1266 cm^{-1} with the increasing CNF content. However, no characteristic peaks of CNF were observed in the spectra of the RSF/CNF fibers. This was probably because the CNF content in the RSF/CNF fibers was very low (up to 0.3 wt %). However, the results of XPS in Table 1 showed that the nitrogen content of RSF fibers was 16.55%, while no nitrogen was found in lyophilized CNF powder. When only 0.3 wt % CNF was added in the RSF/CNF-3 fiber, the nitrogen content decreased to 12.15%. Obviously, the N/C ratio decreased significantly from 0.28 to 0.19, which proved that CNF was in the hybrid RSF/CNF fibers.

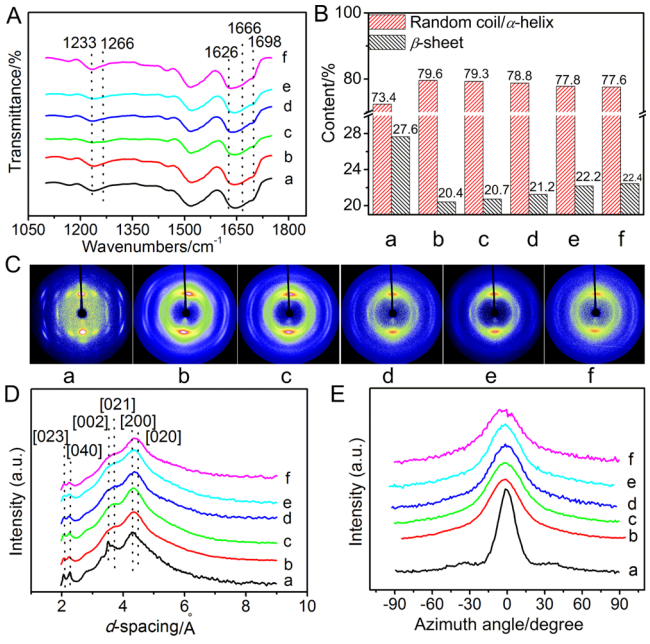

Figure 9. Structure analysis of a variety of silk fibers: (a) De-silk, (b) RSF, (c) RSF/CNF-0.5, (d) RSF/CNF-1, (e) RSF/CNF-2, and (f) RSF/CNF-3 using FTIR and WAXD techniques. (A) FTIR spectra, (B) deconvolution result of the FTIR spectra for the amide III band, (C) 2D SR-WAXD patterns, and (D) 1D integrated WAXD profile from (C,E) the azimuthal intensity profiles at the [200] peak position.

Table 1. Carbon Content, Oxygen Content, Nitrogen Content, and the N/C Ratio of the RSF Fiber, RSF/CNF-3 Fiber, and CNF Powder

sample	carbon content (%)	oxygen content (%)	nitrogen content (%)	N/C ratio
RSF	60	23.45	16.55	0.28
RSF/CNF-3	65.38	22.48	12.15	0.19
CNF	55.53	44.47	0	0

To quantitatively investigate the protein conformation transition of each sample, spectra deconvolution was carried out to analyze the amide III band (Figure S2). The deconvolution results are shown in Figure 9B. The results indicated that the β-sheet content in the hybrid silks was slightly higher than that of RSF fibers but lower than that of De-silk. This suggests that the addition of CNF is favorable for the conformation transition of RSF molecules from random

DOI: 10.1021/acssuschemeng.9b02713
ACS Sustainable Chem. Eng. 2019, 7, 14765−14774

Table 2. Structure Parameters Extracted from the WAXD Analysis for De-Silk and RSF/CNF Fibers[a,b]

sample	$f_{crystal}$	$f_{mesophase}$	crystallinity (%)	mesophase content (%)	crystallite size (nm)		
					(200)/(210)	(020)	(002)
De-silk	0.97	0.60	55.1	14.7	4.2	3.2	8.9
RSF	0.94	0.64	50.8	14.9	3.9	3.8	3.6
RSF/CNF-0.5	0.95	0.64	50.8	12.9	3.8	3.6	2.8
RSF/CNF-1	0.95	0.62	51.5	14.3	3.7	3.6	2.7
RSF/CNF-2	0.93	0.59	52.6	15.9	3.6	3.5	2.6
RSF/CNF-3	0.91	0.58	52.9	18.4	3.6	3.5	2.7

[a] $f_{crystal}$: Herman's orientation of the crystal domains. [b] $f_{mesophase}$: Herman's orientation of the mesophase domains.

coil or α-helix to β-sheet. One possible reason was that the alignment of CNF promoted the extension of the RSF chains. This is certainly consistent with the finding that the β-sheet content of all hybrid fibers was larger than that of the neat RSF fiber. Furthermore, the β-sheet content in the hybrid silk fibers was found to increase with the increase of CNF content, while the random coil/α-helix conformation decreased. This finding agreed with the results of Liu et al.[32] in the study of the wet-spun CNC/silk hybrid fibers. In the case of the very low CNF content (e.g., 0.05 wt %), the loose CNF network did not severely restrict the mobility of RSF chains, which means that RSF chains would have sufficient time to rearrange during spinning. With the increase of the CNF content, the CNF network became denser, which probably reduced the mobility of RSF chains. The strong interactions between CNF and RSF could thus result in the enhanced β-sheet conformation. In a way, CNF seemed to behave as the cross-linking β-sheet crystallite in the RSF/CNF fiber, mimicking the crystalline structure in natural silk.[32] SR-WAXD measurements were carried out to study the crystal structure and orientation of a variety of fibers (De-silk and RSF/CNF fibers with different composition ratios). Such information could be related to the mechanical properties.[51−53] The initial 2D SR-WAXD pattern and the deconvolution of 1D SR-WAXD diffractograms of the chosen fibers are shown in Figures 9C and S2, respectively. It was seen that the SR-WAXD patterns of RSF/CNF fibers are very different from that of the De-silk fibers. Figure 9D,E illustrates the SR-WAXD profiles and the azimuth scan of the [200] lattice plane for these fibers, respectively. These results are discussed below.

The structure parameters extracted from the WAXD analysis of the different fibers are summarized in Table 2. These parameters include Herman's orientation factors for both crystalline and amorphous domains, crystallinity, mesophase content, and crystallite sizes estimated from different diffraction planes. It was found that the crystallinity of the RSF/CNF fibers was higher than that of the RSF fiber. This indicated that a more ordered crystalline structure was induced by the presence of CNF, which was consistent with the FTIR result. As CNF could play the role of the β-sheet crystallite in RSF/CNF fibers, the higher CNF content would result in a higher RSF crystalline content. However, the crystallinity of all RSF-based fibers was found to be smaller than that of De-silk.

The mesophase content in the silk fiber has been defined in our previous work.[14] The result of the mesophase content is shown in Table 2. It was found that the mesophase content in RSF/CNF fibers also increased with the increase of CNF. For RSF/CNF-2 and RSF/CNF-3, the mesophase content was larger than that of RSF and De-silk fibers. The mesophase may be related to the interface between interactions between RSF and CNF, leading to the formation of RSF/CNF. It has been shown that the mesophase can play an important role in enhancing the mechanical properties of the hybrid fibers.[54] It is conceivable that during the stretching process, the mesophase between the RSF amorphous domain and CNF can contribute to the plastic flow under large tensile strain, which would result in a large strain to break ratio and enhance the strength of the hybrid fibers.

The Herman's orientation factors of the crystal phase (f_c) and the mesophase (f_m) are also shown in Table 2. It was seen that the f_c values of RSF/CNF-0.5 and RSF/CNF-1 fibers were larger than that of the RSF silk, indicating that the addition of CNF promoted the orientation of RSF molecules, leading to a slightly higher degree of orientation of the crystal domain. However, with the increasing CNF content, the charged CNF formed a gel state, which could not be easily oriented by stretching. As a result, f_c decreased slightly (e.g., 0.93 and 0.91 for RSF/CNF-2 and RSF/CNF-3, respectively). The f_m value of the RSF/CNF-0.5 fiber was found to be close to that of RSF, probably due to the low content of the mesophase content. With the increase of the CNF content, the mesophase content increased, but the f_m value decreased. This might be because the high degree of cross-linking due to charged CNF could restrict the mobility of the mesophase during stretching.

The position of the [210]/[200], [020], and [002] diffraction peaks and the full width at half-maxima of these peaks were used to determine the crystallite sizes along the a, b, and c directions, respectively, using the Scherer equation. It was found that the RSF/CNF fibers generally exhibited smaller crystallite sizes than De-silk and RSF fibers. Furthermore, the crystallite size showed a notable decrease with the increase of the CNF content. This may be because when the RSF chains were tethered to CNF, they could be oriented rapidly along the fiber axis during the extrusion/stretching process. The higher CNF content results in the higher population of the oriented chain. This can lead to higher crystal orientation and larger crystallinity as well as the improved tensile strength in the RSF/CNF fiber,[45] but the resulting crystallite size is generally smaller because of the confined RSF domains.

On the basis of the above results, we argued two major reasons to explain the reinforcement effect of CNF in the RSF/CNF hybrid fibers. First, CNF generally acted as an anisotropic additive, leading to higher molecular orientations of both fillers and the matrix molecules under deformation and thus higher fiber strength. Second, the formation of intermolecular hydrogen bonds between CNF (e.g., carboxyl groups and hydroxyl group) and RSF (e.g., amino groups) further enhanced the interfacial RSF molecular orientation under deformation, resulting in higher crystallinity and higher crystalline orientation. However, the confinement of the tethered RSF chains on the surface of CNF also led to higher mesophase content and smaller crystallite size.

DOI: 10.1021/acssuschemeng.9b02713
ACS Sustainable Chem. Eng. 2019, 7, 14765−14774

CONCLUSIONS

We demonstrated a simple and environmentally friendly process to fabricate RSF/CNF hybrid fibers with notably enhanced mechanical properties. In specific, the RSF/CNF hybrid fibers spun through a microfluidic channel, which mimicked the shape of the major ampullate gland of spiders, using the RSF aqueous solution with the addition of CNF could result in higher crystallinity, higher mesophase content, and smaller crystallite size but higher mechanic performance. For example, the breaking strength of the RSF/CNF fiber with 0.1 wt % CNF was found to be around 486 ± 106 MPa, with a 58% increase over the neat RSF fiber and a maximum value of 686 MPa, drastically exceeding that of silkworm silks. The enhanced mechanical properties could be explained by the synergistic effect of the network structure formed by the CNF particles and the interactions (e.g., hydrogen bonds) between the CNF and RSF molecules. This study demonstrates a new strategy to design and fabricate high-performance artificial silk fibers.

ASSOCIATED CONTENT

Supporting Information

The Supporting Information is available free of charge on the ACS Publications website at DOI: 10.1021/acssuschemeng.9b02713.

Characterizations for the De-silk and RSF/CNF fibers; deconvolution of FTIR in the amide III band; mechanical properties of De-silk and RSF/CNF fibers; and deconvolution of 1D SR-WAXD diffractograms of De-silk and RSF/CNF fibers (PDF)

AUTHOR INFORMATION

Corresponding Authors

*E-mail: benjamin.hsiao@stonybrook.edu (B.S.H.).
*E-mail: zyp@dhu.edu.cn (Y.Z.).

ORCID

Suna Fan: 0000-0001-6508-360X
Benjamin S. Hsiao: 0000-0002-3180-1826
Yaopeng Zhang: 0000-0002-7175-6150

Present Address

‖School of Life Sciences and Biotechnology, Shanghai Jiao Tong University, Shanghai 200240, China.

Author Contributions

Y.Z. conceived and directed the research. L.L. fabricated the hybrid fiber, performed all the characterization, and wrote the manuscript. Q.N. and L.G. assisted the SAXS measurement of CNF suspension. B.S.H. and S.F. joined the WAXD and SAXS analysis. Q.P. designed the microfluidic chip. H.S. and G.Y. directed the FTIR analyses of silk fibroin. All authors have given approval to the final version of the manuscript.

Notes

The authors declare no competing financial interest.

ACKNOWLEDGMENTS

This work was sponsored by the National Key Research and Development Program of China (2016YFA0201702/2016YFA0201700), the Fundamental Research Funds for the Central Universities (2232019A3-06, 2232019D3-02), the National Key Research and Development Program of China (2018YFC1105802/2018YFC1105800), the National Natural Science Foundation of China (21674018), the Shanghai Belt and Road Joint Laboratory of Advanced Fiber and Low-dimension Materials (18520750400), Programme of Introducing Talents of Discipline to Universities (No. 111-2-04), and the National Science Foundation in the U.S. (DMR-1808690).

REFERENCES

(1) Lin, Z.; Deng, Q.; Liu, X.-Y.; Yang, D. Engineered Large Spider Eggcase Silk Protein for Strong Artificial Fibers. *Adv. Mater.* **2013**, *25*, 1216−1220.
(2) Rising, A.; Johansson, J. Toward Spinning Artificial Spider Silk. *Nat. Chem. Biol.* **2015**, *11*, 309−315.
(3) Vollrath, F. Strength and Structure of Spiders' Silks. *J. Biotechnol.* **2000**, *74*, 67−83.
(4) Zhou, G.; Shao, Z.; Knight, D. P.; Yan, J.; Chen, X. Silk Fibers Extruded Artificially from Aqueous Solutions of RegeneratedBombyx moriSilk Fibroin are Tougher than their Natural Counterparts. *Adv. Mater.* **2009**, *21*, 366−370.
(5) Omenetto, F. G.; Kaplan, D. L. New Opportunities for an Ancient Material. *Science* **2010**, *329*, 528−531.
(6) Koeppel, A.; Holland, C. Progress and Trends in Artificial Silk Spinning: a Systematic Review. *ACS Biomater. Sci. Eng.* **2017**, *3*, 226−237.
(7) FAOSTAT-Food and Agriculture Organization of the United Nations Statistics Division. http://www.fao.org/faostat/zh/#data (accessed July 15, 2019).
(8) Chen, Z.; Zhang, H.; Lin, Z.; Lin, Y.; van Esch, J. H.; Liu, X. Y. Programing Performance of Silk Fibroin Materials by Controlled Nucleation. *Adv. Funct. Mater.* **2016**, *26*, 8978−8990.
(9) Fang, G.; Huang, Y.; Tang, Y.; Qi, Z.; Yao, J.; Shao, Z.; Chen, X. Insights into Silk Formation Process: Correlation of Mechanical Properties and Structural Evolution during Artificial Spinning of Silk Fibers. *ACS Biomater. Sci. Eng.* **2016**, *2*, 1992−2000.
(10) Peng, Q.; Shao, H.; Hu, X.; Zhang, Y. Role of Humidity on the Structures and Properties of Regenerated Silk Fibers. *Prog. Nat. Sci.: Mater. Int.* **2015**, *25*, 430−436.
(11) Yue, X.; Zhang, F.; Wu, H.; Ming, J.; Fan, Z.; Zuo, B. A Novel Route to Prepare Dry-Spun Silk Fibers from $CaCl_2$-Formic Acid Solution. *Mater. Lett.* **2014**, *128*, 175−178.
(12) Guzman-Puyol, S.; Heredia-Guerrero, J. A.; Ceseracciu, L.; Hajiali, H.; Canale, C.; Scarpellini, A.; Cingolani, R.; Bayer, I. S.; Athanassiou, A.; Mele, E. Low-Cost and Effective Fabrication of Biocompatible Nanofibers from Silk and Cellulose-Rich Materials. *ACS Biomater. Sci. Eng.* **2016**, *2*, 526−534.
(13) Pan, H.; Zhang, Y.; Hang, Y.; Shao, H.; Hu, X.; Xu, Y.; Feng, C. Significantly Reinforced Composite Fibers Electrospun from Silk Fibroin/Carbon Nanotube Aqueous Solutions. *Biomacromolecules* **2012**, *13*, 2859−2867.
(14) Zhang, C.; Zhang, Y.; Shao, H.; Hu, X. Hybrid Silk Fibers Dry-Spun from Regenerated Silk Fibroin/Graphene Oxide Aqueous Solutions. *ACS Appl. Mater. Interfaces* **2016**, *8*, 3349−3358.
(15) Pan, H.; Zhang, Y.; Shao, H.; Hu, X.; Li, X.; Tian, F.; Wang, J. Nanoconfined Crystallites Toughen Artificial Silk. *J. Mater. Chem. B* **2014**, *2*, 1408−1414.
(16) Asakura, T.; Umemura, K.; Nakazawa, Y.; Hirose, H.; Higham, J.; Knight, D. Some Observations on the Structure and Function of the Spinning Apparatus in the Silkworm Bombyxmori. *Biomacromolecules* **2007**, *8*, 175−181.
(17) Knight, D. P.; Vollrath, F. Liquid Crystals and Flow Elongation in a Spider's Silk Production Line. *Proc. R. Soc. Ser. B* **1999**, *266*, 519−523.
(18) Breslauer, D. N.; Lee, L. P.; Muller, S. J. Simulation of Flow in the Silk Gland. *Biomacromolecules* **2009**, *10*, 49−57.
(19) Lefevre, T.; Boudreault, S.; Cloutier, C.; Pezolet, M. Conformational and Orientational Transformation of Silk Proteins in the Major Ampullate Gland of Nephila clavipes Spiders. *Biomacromolecules* **2008**, *9*, 2399−2407.

DOI: 10.1021/acssuschemeng.9b02713
ACS Sustainable Chem. Eng. 2019, 7, 14765−14774

(20) Sparkes, J.; Holland, C. Analysis of the Pressure Requirements for Silk Spinning Reveals a Pultrusion Dominated Process. *Nat. Commun.* **2017**, *8*, 594−604.
(21) Xin, G.; Zhu, W.; Deng, Y.; Cheng, J.; Zhang, L. T.; Chung, A. J.; De, S.; Lian, J. Microfluidics-Enabled Orientation and Microstructure Control of Macroscopic Graphene Fibres. *Nat. Nanotechnol.* **2019**, *14*, 168−175.
(22) Rammensee, S.; Slotta, U.; Scheibel, T.; Bausch, A. R. Assembly Mechanism of Recombinant Spider Silk Proteins. *Proc. Natl. Acad. Sci. U.S.A.* **2008**, *105*, 6590−6595.
(23) Chae, S.-K.; Kang, E.; Khademhosseini, A.; Lee, S.-H. Micro/Nanometer-Scale Fiber with Highly Ordered Structures by Mimicking the Spinning Process of Silkworm. *Adv. Mater.* **2013**, *25*, 3071−3078.
(24) Luo, J.; Zhang, L.; Peng, Q.; Sun, M.; Zhang, Y.; Shao, H.; Hu, X. Tough Silk Fibers Prepared in Air Using a Biomimetic Microfluidic Chip. *Int. J. Biol. Macromol.* **2014**, *66*, 319−324.
(25) Peng, Q.; Zhang, Y.; Lu, L.; Shao, H.; Qin, K.; Hu, X.; Xia, X. Recombinant Spider Silk from Aqueous Solutions via a Bio-Inspired Microfluidic Chip. *Sci. Rep.* **2016**, *6*, 36473−36485.
(26) Kinahan, M. E.; Filippidi, E.; Köster, S.; Hu, X.; Evans, H. M.; Pfohl, T.; Kaplan, D. L.; Wong, J. Tunable Silk: Using Microfluidics to Fabricate Silk Fibers with Controllable Properties. *Biomacromolecules* **2011**, *12*, 1504−1511.
(27) Kang, E.; Jeong, G. S.; Choi, Y. Y.; Lee, K. H.; Khademhosseini, A.; Lee, S.-H. Digitally Tunable Physicochemical Coding of Material Composition and Topography in Continuous Microfibres. *Nat. Mater.* **2011**, *10*, 877−883.
(28) Peng, Q.; Shao, H.; Hu, X.; Zhang, Y. The Development of Fibers that Mimic the Core-Sheath and Spindle-Knot Morphology of Artificial Silk Using Microfluidic Devices. *Macromol. Mater. Eng.* **2017**, *302*, 1700102−1700109.
(29) Daniele, M. A.; Boyd, D. A.; Adams, A. A.; Ligler, F. S. Microfluidic Strategies for Design and Assembly of Microfibers and Nanofibers with Tissue Engineering and Regenerative Medicine Applications. *Adv. Healthcare Mater.* **2015**, *4*, 11−28.
(30) Kiriya, D.; Kawano, R.; Onoe, H.; Takeuchi, S. Microfluidic Control of The Internal Morphology in Nanofiber-Based Macroscopic Cables. *Angew. Chem., Int. Ed. Engl.* **2012**, *51*, 7942−7947.
(31) Gandhi, M.; Yang, H.; Shor, L.; Ko, F. Post-Spinning Modification of Electrospun Nanofiber Nanocomposite from *Bombyx Mori Silk* and Carbon Nanotubes. *Polymer* **2009**, *50*, 1918−1924.
(32) Liu, L.; Yang, X.; Yu, H.; Ma, C.; Yao, J. Biomimicking the structure of silk fibers via cellulose nanocrystal as β-sheet crystallite. *RSC Adv.* **2014**, *4*, 14304−14313.
(33) Song, J.; Chen, C.; Zhu, S.; Zhu, M.; Dai, J.; Ray, U.; Li, Y.; Kuang, Y.; Li, Y.; Quispe, N.; Yao, Y.; Gong, A.; Leiste, U. H.; Bruck, H. A.; Zhu, J. Y.; Vellore, A.; Li, H.; Minus, M. L.; Jia, Z.; Martini, A.; Li, T.; Hu, L. Processing Bulk Natural Wood into a High-Performance Structural Material. *Nature* **2018**, *554*, 224−228.
(34) Ling, S.; Kaplan, D. L.; Buehler, M. J. Nanofibrils in Nature and Materials Engineering. *Nat. Rev. Mater.* **2018**, *3*, 18016−18031.
(35) Mittal, N.; Jansson, R.; Widhe, M.; Benselfelt, T.; Håkansson, K. M. O.; Lundell, F.; Hedhammar, M.; Söderberg, L. D. Ultrastrong and Bioactive Nanostructured Bio-Based Composites. *ACS Nano* **2017**, *11*, 5148−5159.
(36) Isogai, A.; Saito, T.; Fukuzumi, H. TEMPO-Oxidized Cellulose Nanofibers. *Nanoscale* **2011**, *3*, 71−85.
(37) Håkansson, K. M. O.; Fall, A. B.; Lundell, F.; Yu, S.; Krywka, C.; Roth, S. V.; Santoro, G.; Kvick, M.; Prahl Wittberg, L.; Wågberg, L.; Söderberg, L. D. Hydrodynamic Alignment and Assembly of Nanofibrils Resulting in Strong Cellulose Filaments. *Nat. Commun.* **2014**, *5*, 4018−4028.
(38) Mittal, N.; Ansari, F.; Gowda.V, K.; Brouzet, C.; Chen, P.; Larsson, P. T.; Roth, S. V.; Lundell, F.; Wågberg, L.; Kotov, N. A.; Söderberg, L. D. Multiscale control of nanocellulose assembly: transferring remarkable nanoscale fibril mechanics to macroscale fibers. *ACS Nano* **2018**, *12*, 6378−6388.
(39) Mortimer, B.; Guan, J.; Holland, C.; Porter, D.; Vollrath, F. Linking Naturally and Unnaturally Spun Silks through the Forced Reeling of Bombyx Mori. *Acta Biomater.* **2015**, *11*, 247−255.
(40) Su, Y.; Burger, C.; Ma, H.; Chu, B.; Hsiao, B. S. Exploring the Nature of Cellulose Microfibrils. *Biomacromolecules* **2015**, *16*, 1201−1209.
(41) Su, Y.; Burger, C.; Hsiao, B. S.; Chu, B. Characterization of TEMPO-Oxidized Cellulose Nanofibers in Aqueous Suspension by Small-Angle X-Ray Scattering. *J. Appl. Crystallogr.* **2014**, *47*, 788−798.
(42) Geng, L.; Peng, X.; Zhan, C.; Naderi, A.; Sharma, P. R.; Mao, Y.; Hsiao, B. S. Structure Characterization of Cellulose Nanofiber Hydrogel as Functions of Concentration and Ionic Strength. *Cellulose* **2017**, *24*, 5417−5429.
(43) Yao, J.; Chen, S.; Chen, Y.; Wang, B.; Pei, Q.; Wang, H. Macrofibers with High Mechanical Performance based on Aligned Bacterial Cellulose Nanofibers. *ACS Appl. Mater. Interfaces* **2017**, *9*, 20330−20339.
(44) Xia, X.-X.; Qian, Z.-G.; Ki, C. S.; Park, Y. H.; Kaplan, D. L.; Lee, S. Y. Native-Sized Recombinant Spider Silk Protein Produced in Metabolically Engineered Escherichia Coli Results in a Strong Fiber. *Proc. Natl. Acad. Sci. U.S.A.* **2010**, *107*, 14059−14063.
(45) Sun, M.; Zhang, Y.; Zhao, Y.; Shao, H.; Hu, X. The Structure−Property Relationships of Artificial Silk Fabricated by Dry-Spinning Process. *J. Mater. Chem.* **2012**, *22*, 18372−18379.
(46) Miller, L. D.; Putthanarat, S.; Eby, R. K.; Adams, W. W. Investigation of the Nanofibrillar Morphology in Silk Fibers by Small Angle X-Ray Scattering and Atomic Force Microscopy. *Int. J. Biol. Macromol.* **1999**, *24*, 159−165.
(47) Kamada, A.; Mittal, N.; Söderberg, L. D.; Ingverud, T.; Ohm, W.; Roth, S. V.; Lundell, F.; Lendel, C. Flow-Assisted Assembly of Nanostructured Protein Microfibers. *Proc. Natl. Acad. Sci. U.S.A.* **2017**, *114*, 1232−1237.
(48) Ling, S.; Qi, Z.; Knight, D. P.; Shao, Z.; Chen, X. Synchrotron FTIR Microspectroscopy of Single Natural Silk Fibers. *Biomacromolecules* **2011**, *12*, 3344−3349.
(49) Chen, X.; Knight, D. P.; Shao, Z. β-Turn Formation during the Conformation Transition in Silk Fibroin. *Soft Matter* **2009**, *5*, 2777−2781.
(50) Chen, X.; Shao, Z.; Knight, D. P.; Vollrath, F. Conformation Transition Kinetics of Bombyx Mori Silk Protein. *Proteins* **2007**, *68*, 223−231.
(51) Riekel, C.; Madsen, B.; Knight, D.; Vollrath, F. X-Ray Diffraction on Spider Silk during Controlled Extrusion under a Synchrotron Radiation X-Ray Beam. *Biomacromolecules* **2000**, *1*, 622−626.
(52) Riekel, C.; Müller, M.; Vollrath, F. In Situ X-Ray Diffraction during Forced Silking of Spider Silk. *Macromolecules* **1999**, *32*, 4464−4466.
(53) Sampath, S.; Isdebski, T.; Jenkins, J. E.; Ayon, J. V.; Henning, R. W.; Orgel, J. P. R. O.; Antipoa, O.; Yarger, J. L. X-Ray Diffraction Study of Nanocrystalline and Amorphous Structure within Major and Minor Ampullate Dragline Spider Silks. *Soft Matter* **2012**, *8*, 6713−6722.
(54) Zhang, C.; Zhang, Y.; Luo, J.; Shi, J.; Shao, H.; Hu, X. Microstructural Evolution of Regenerated Silk Fibroin/Graphene Oxide Hybrid Fibers under Tensile Deformation. *RSC Adv.* **2017**, *7*, 3108−3116.

DOI: 10.1021/acssuschemeng.9b02713
ACS Sustainable Chem. Eng. 2019, 7, 14765−14774